Controlling viral capsid assembly with templating

Michael F. Hagan
Department of Physics, Brandeis University, Waltham, Massachusetts, 02454, USA
(Received 19 December 2007; published 8 May 2008)

We develop coarse-grained models that describe the dynamic encapsidation of functionalized nanoparticles by viral capsid proteins. We find that some forms of cooperative interactions between protein subunits and nanoparticles can dramatically enhance rates and robustness of assembly, as compared to the spontaneous assembly of subunits into empty capsids. For large core-subunit interactions, subunits adsorb onto core surfaces en masse in a disordered manner, and then undergo a cooperative rearrangement into an ordered capsid structure. These assembly pathways are unlike any identified for empty capsid formation. Our models can be directly applied to recent experiments in which viral capsid proteins assemble around functionalized inorganic nanoparticles [Sun *et al.*, Proc. Natl. Acad. Sci. U.S.A. **104**, 1354 (2007)]. In addition, we discuss broader implications for understanding the dynamic encapsidation of single-stranded genomic molecules during viral replication and for developing multicomponent nanostructured materials.

DOI: 10.1103/PhysRevE.77.051904 PACS number(s): 87.15.A−, 64.75.Yz, 81.16.Dn, 87.10.Tf

I. INTRODUCTION

The assembly of simple building blocks into larger, ordered structures is crucial for many biological processes and is enabling manufacture of novel nanostructured materials (e.g., ([1–7]), which often draw inspiration and materials from biology. The spontaneous assembly of viral proteins into empty capsids (protein shells) has been the subject of elegant *in vitro* experiments (e.g., [8–17]) and insightful theoretical works (e.g., [18–31]). The *in vivo* replication of many viruses, however, involves simultaneous assembly and encapsidation of the viral genome [32]. Likewise, many nanostructured materials require precise spatial ordering of multiple, dissimilar components. In this paper, we develop coarse-grained models for a particular example of multicomponent assembly—the assembly of viral capsid proteins around a rigid spherical template. Our models predict that a template enables increased assembly rates and efficient assembly over a wider range of parameters that control assembly driving forces, as compared to the spontaneous assembly of empty capsids. We find that template properties can control assembly pathways, and our models predict a mechanism that is unique to multicomponent assembly.

Our models are motivated by recent experiments in which Brome mosaic virus (BMV) capsid proteins dynamically encapsidate functionalized inorganic nanoparticle cores, creating unique biological and synthetic composite structures called viruslike particles (VLPs) [33–36]. By combining the unparalleled self-assembly and targeting capabilities of viruses with the functionalizability of nanoparticles, VLPs show promise as imaging agents [36–39], diagnostic and therapeutic vectors [40–42], and as subunits or templates for synthesis of advanced nanomaterials [43–46]. Our models offer a framework with which to interpret experimental results in order to design more efficient templated assembly of nanomaterials, and a means to use this as a model system with which to understand aspects of viral protein assembly around nucleic acid cores.

Formation of the hollow shell geometry of a capsid poses a significant challenge that requires anisotropic, directional interactions between subunits. Thus, in addition to their biomedical and technological applications, the study of viral capsids has revealed fundamental principles of assembly. Although specific assembly mechanisms are poorly understood for most viruses, a general mechanism has emerged for the spontaneous assembly of empty capsids [10–15,21,26,28,47–54]. Assembly occurs through a sequential addition process in which individual subunits or larger intermediates [26,52] bind to a growing capsid. Assembly rates must be restrained to avoid two forms of kinetic traps (long-lived metastable states): (a) if new intermediates form too rapidly, the pool of free subunits becomes depleted before most capsids finish assembling [12,21,26,47,48,52,53], (b) malformed structures result when additional subunits bind more rapidly than strained bonds can anneal within a partial capsid [26,28,55,56]. The formation of too many partial capsids can be suppressed by a slow nucleation step [48], but avoidance of both sources of kinetic frustration requires relatively weak subunit-subunit binding free energies [26,28,29,47,48,57]. Theoretical work suggests that weak binding free energies are a general requirement for successful assembly into an ordered low free energy product; binding free energies that are large compared to the thermal energy (k_BT) prevent the system from "locally" equilibrating between different metastable configurations during assembly [51,57,58].

Although *in vitro* studies of empty capsids provide a foundation for understanding assembly, interaction of proteins with a central "core" is crucial for the replication of many viruses in their native environments, where capsid proteins must encapsidate the viral genome during assembly [32]. There is no role for exogenous species in the sequential assembly mechanism discussed above, but *in vitro* capsid assembly experiments in the presence of RNA demonstrate different kinetics than capsid proteins alone, and suggest the presence of protein-RNA intermediates [59].

Prior theoretical and computational studies of multicomponent assembly have examined the equilibrium behavior of polyelectrolyte encapsidation [60–64] and the equilibrium configurations of colloids confined to convex surfaces [27,65]. A qualitative kinetic model has been proposed to

explain the formation of icosahedral symmetry in encapsidated RNA [66] and Hu and Shklovskii [67] considered a model in which capsid proteins nonspecifically bind to single-stranded RNA and slide on it toward an assembling capsid at one end, which increases the rate of assembly. While increased binding rates are one possible feature of multicomponent assembly, an interior core, such as a nucleic acid or nanoparticle, may also promote assembly by acting as a template that steers assembly toward certain morphologies and as a heterogeneous nucleation site that localizes capsid proteins in an environment favorable for assembly. These factors may generate assembly mechanisms that are entirely different from the sequential mechanism considered in the formation of empty capsids. For instance, McPherson [68] proposed a qualitative model in which a large number of proteins nonspecifically bind to a nucleic acid molecule to form a structure resembling a reverse micelle, and then reorient to form an ordered capsid. In this work we present a computational model for the encapsidation of an interior core with no preassumed pathways. For some sets of system parameters, our simulations predict assembly mechanisms consistent with McPherson's model.

In addition to the technological applications discussed above, solid nanoparticles offer a simplified, controllable experimental system with which to test models for the effect of heterogeneous nucleation and templating on assembly, and thus may lead to valuable insights about viral assembly around nucleic acid cores as well as elucidate the fundamental principles of multicomponent assembly. Experiments show that capsid assembly around cores competes with spontaneous assembly at subunit concentrations well above the threshold concentration for empty capsid assembly [critical subunit concentration (CSC)] [33], and that assembly occurs in the presence of cores below the CSC [69]. These results point to the ability of nanoparticles to act as heterogeneous nucleation agents. In addition, nanoparticles promote formation of capsid morphologies that are commensurate with nanoparticle sizes, which suggests that cores can direct the final assembly product through templating. The time dependence of the mass-averaged amount of proteins on cores can be estimated by light scattering [69], but is not possible to characterize the extent to which these proteins have assembled without static procedures, such as crystallography or electron microscopy. Kinetic models that relate assembly pathways to dynamical observables such as light scattering are therefore necessary to understand assembly mechanisms.

In this work, we present a computational model for assembly around solid cores, with which we analyze kinetics and assembly pathways as functions of the parameters that control the driving forces of assembly, including subunit concentrations, subunit-subunit binding energies, and surface adsorption free energies. At low adsorption free energies and/or low subunit concentrations, assembly mechanisms resemble those seen for empty capsids, whereas assembly pathways at high adsorption free energies and/or subunit concentrations resemble the reverse micelle model. We demonstrate that the effect of cores on rates and assembly mechanisms can be understood through simple and general scaling arguments.

II. MODEL

We consider a dilute solution of capsid subunits with a reduced concentration $C_s=\rho\sigma^3$, with ρ the number density and σ the subunit diameter, and rigid cores with a reduced concentration C_C. Subunits can spontaneously assemble to form empty shells with well-defined structures of size N subunits. In addition, subunits interact favorably with cores and thus adsorb to, and assemble on, core surfaces. Complete assembly of adsorbed subunits results in core encapsidation. Our models are motivated by the experiments described above in which viral capsid proteins assemble on inorganic nanoparticles; thus, we begin by adapting a model previously used to simulate the spontaneous assembly of empty capsids [26]. This computational model is general, however, and could describe, for example, colloidal subunits with directional interactions [70–72]. Likewise, the scaling arguments below are general enough to describe many forms of simultaneous assembly and cargo encapsidation for systems in which cargo degrees of freedom change slowly in comparison to assembly timescales.

A. Modeling empty capsid formation

We imagine integrating over microscopic degrees of freedom as capsid proteins fluctuate about their native states, to arrive at a pairwise decomposable model in which subunits have spherically symmetric excluded volumes and directionally specific, short ranged attractions between complementary interfaces. The lowest energy states in the model correspond to separate "capsids," which consist of multiples of 60 monomers in a shell with icosahedral symmetry. In this work we model experiments in which BMV capsid proteins assemble around 6 nm nanoparticles, for which only T1 capsid geometries are observed [33]. Because the basic assembly unit of BMV is a dimer [73–75], our model subunit represents a protein dimer. Our energy minimum model capsid therefore is comprised of 60 monomers or $N=30$ dimer subunits arranged with icosahedral symmetry, as shown in Fig. 1.

The locations of subunit interfaces are tracked by internal bond vectors $\mathbf{b}_i^{(\alpha)}$, which are fixed rigidly within a subunit frame of reference, with $\alpha\in\{1,2,\ldots,n_b\}$ and n_b is the number of interfaces on each subunit. In this work there are $n_b=4$ bond vectors that can be represented in Cartesian coordinates as $\mathbf{b}_i^{(\alpha)}/b=0.5k_x^\alpha\hat{\mathbf{x}}+0.809k_y^\alpha\hat{\mathbf{y}}+0.309\hat{\mathbf{z}}$ with the bond length $b=2^{-5/6}$ and $k_x=\{1,-1,-1,1\}$ and $k_y=\{1,1,-1,-1\}$, so that the angles between bond vectors have the values indicated in Fig. 1(a) and the minimum energy capsids have 30 subunits as shown in Fig. 1(b). This model results from merging pairs of monomeric subunits in the B5 capsid model considered in Ref. [26] (see Fig. 1 in that reference) and the resulting model capsid has the same connectivity as a model considered by Endres *et al.* [48] [see Fig. 1B in that reference].

The interaction between subunits i and j is

$$u_{ij}=u_{\mathrm{rep}}(|\mathbf{R}_i-\mathbf{R}_j|)+{\sum_{\alpha\beta}}'u_{\mathrm{att}}(|\mathbf{r}_i^{(\alpha)}-\mathbf{r}_j^{(\beta)}|)\times s_{\alpha\beta}(\theta_{ij}^{(\alpha,\beta)},\theta_m)s_{\alpha,\beta}(\phi_{ij}^{(\gamma,\epsilon)},\phi_m),\quad(1)$$

where $\mathbf{R}_i$ is the center of subunit i and $\mathbf{r}_i^{(\alpha)}\equiv\mathbf{R}_i+\mathbf{b}_i^{(\alpha)}$ is the

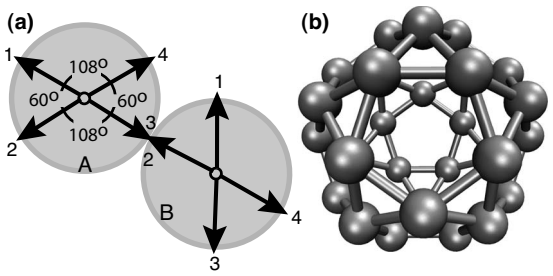

FIG. 1. (a) Geometry of subunits and attractive interactions for the computational model. Bond vectors are depicted as arrows; bond vector 3 on subunit A and bond vector 2 on subunit B have an attractive interaction if they are nearly antiparallel and the secondary bond vectors, bond vector 2 on subunit A and bond vector 3 on subunit B, are nearly coplanar. The angles between indicated bond vectors are specified in degrees. (b) The low free energy capsid geometry. The center of each subunit roughly corresponds to a twofold axis of symmetry (at dimer interfaces) in a BMV T1 capsid (see Ref. [78] and the VIPER database [79]). Subunit sizes are reduced to aid visibility.

position of the interface represented by bond vector α on subunit i. The repulsive excluded volume interaction is

$$u_{\mathrm{rep}}(R) = \Theta(r_{\mathrm{m}} - R)[1 + \mathcal{L}(R/\sigma)], \tag{2}$$

where we have defined a Lennard-Jones function $\mathcal{L}(x) = 4(x^{-12} - x^{-6})$ and $\Theta(x)$ is the step function with $r_{\mathrm{m}} \equiv 2^{1/6}\sigma$ the maximum range of the repulsion.

The attractive interactions depend on the relative configurations and alignments of complementary interfaces. To reflect this, the sum in Eq. (1) is marked with a prime to note that it runs over all pairs of complementary interfaces, which in this work are all pairings of bond vectors with an even and odd label, e.g., $(\alpha, \beta) = (1,4)$ or (3,2). These pairs are denoted *primary* interactions. A favorable interaction between a pair of complementary interfaces has three requirements [see Fig. 1(a)]. First, the interfaces should closely approach each other, which is enforced by the distance potential

$$u_{\mathrm{att}}(r) = \varepsilon_{\mathrm{b}}\Theta(r_{\mathrm{c}} - \hat{r})[\mathcal{L}(\hat{r}/\sigma) - \mathcal{L}(r_{\mathrm{c}}/\sigma)] \tag{3}$$

with $r_{\mathrm{c}} = 2.5$ the cutoff distance, ε_{b} the strength of the attractive interaction, and $\hat{r} \equiv r + r_{\mathrm{m}}$ a shifted distance so that the minimum of the potential occurs at $r = 0$. The second requirement for a favorable interaction is that primary bond vectors $\mathbf{b}_i^{(\alpha)}$ and $\mathbf{b}_j^{(\beta)}$ are aligned antiparallel, which is enforced by the third factor in Eq. (1) with

$$\cos(\theta_{ij}^{(\alpha,\beta)}) = -\mathbf{b}_i^{(\alpha)} \cdot \mathbf{b}_j^{(\beta)}/b^2. \tag{4}$$

The tolerance of the potential to angular fluctuations is controlled by the specificity function $s_{\alpha\beta}$:

$$s_{\alpha\beta}(\psi, \psi_{\mathrm{m}}) \equiv \frac{1}{2}\Theta(\psi_{\mathrm{m}} - \psi)[\cos(\pi\psi/\psi_{\mathrm{m}}) + 1] \tag{5}$$

where $\psi = \theta$ or ϕ for primary or secondary interactions (defined next), respectively, and ψ_{m} is the maximum angle deviation, which controls the angular specificity of the attractive interactions. In this work, we vary the primary bond angle tolerance θ_{m} from 0.25 to 2.5 rad.

The third requirement for an attractive interaction is that two *secondary* bond vectors, which are not involved in the primary interaction, are coplanar. This requirement enforces angular specificity in the direction azimuthal to the primary bond vectors. A specific pair of secondary bond vectors (γ, ϵ) is associated with each primary pair (α, β), and the second angular factor in Eq. (1) favors the alignment of the normals to two planes. The first plane is defined by the intersubunit vector $\mathbf{R}_{ij} \equiv \mathbf{R}_i - \mathbf{R}_j$ and the first member of the secondary pair, $\mathbf{b}_i^{(\gamma)}$; the second plane is defined by $\mathbf{R}_{ij}$ and the second member of the same secondary pair, $\mathbf{b}_j^{(\epsilon)}$. Denoting these normals by $\mathbf{n}_i^{\gamma} \equiv \mathbf{b}_i^{(\gamma)} \times \mathbf{R}_{ij}$ and $\mathbf{n}_j^{\epsilon} \equiv \mathbf{b}_j^{(\epsilon)} \times \mathbf{R}_{ij}$, the dihedral angle ϕ in Eq. (1) is determined from

$$\cos(\phi_{ij}^{\alpha,\beta}) = \hat{\mathbf{n}}_i^{(\gamma)} \cdot \hat{\mathbf{n}}_j^{(\epsilon)} \tag{6}$$

with $\hat{\mathbf{n}}$ the unit vector $\mathbf{n}/|n|$.

Subunit positions and orientations are propagated according to overdamped Brownian dynamics, with the unit of time $t_0 = \sigma^2/48D$, where D is the subunit diffusion coefficient. All energies are measured in units of the thermal energy $k_{\mathrm{B}}T$. In this work, secondary pairs are specified as the inverse of the primary pairs: $(\gamma, \epsilon) = (\beta, \alpha)$, and the dihedral specificity parameter $\phi_{\mathrm{m}} = \pi$ rad throughout. We vary the subunit concentration over the range $C_{\mathrm{S}} \in [2 \times 10^{-3}, 4 \times 10^{-2}]$. If we choose the diameter of the dimer subunit to be $\sigma = 5$ nm, these concentrations correspond to $27 - 540\ \mu M$.

We note that Nguyen and co-workers [28] recently developed a model for capsid subunits in which subunit excluded volumes have a roughly trapezoidal shape. Interestingly, the assembly kinetics predicted by their model are qualitatively similar to those of the model described above [26], except that they find insertion of the final subunit (to form a complete capsid) is uphill in free energy for many sets of parameters. While insertion of the final subunit is also slowed by excluded volume constraints for the present model, we find that, once completed, capsids are stable and dissociation of a subunit is slow compared to assembly time scales. This result seems consistent with experimental observations that subunit exchange between completed P22 capsids and free subunits is characterized by long time scales (days) compared to those for assembly (minutes) [76,77].

B. Modeling nanoparticle encapsidation

We modify the empty capsid model by introducing a nanoparticle, or a rigid sphere, with radius R_{C} at a fixed position at the center of the simulation cell $\mathbf{C}$. In addition to the pairwise interactions between subunits described above, subunits interact with the nanoparticle via excluded volume interactions and attractive interactions. The potential energy of interaction $u_{\mathrm{c}}(|\mathbf{R} - \mathbf{C}|)$ between a subunit at position R and the nanoparticle is a spherically symmetric shifted Lennard-Jones potential

$$u_{\mathrm{c}}(r) = \varepsilon_{\mathrm{c}}\Theta(r_{\mathrm{c}} - \hat{r})[\mathcal{L}(\hat{r}/\sigma) - \mathcal{L}(r_{\mathrm{c}}/\sigma)], \tag{7}$$

where $r_{\mathrm{c}} = 2.5$ is the cutoff distance. The strength of the attractive interaction is dictated by ε_{c} and $\hat{r} = r - (R_{\mathrm{C}} - 0.5)$ is a shifted distance so that the attraction has its minimum value, $-\varepsilon_{\mathrm{c}} - u_{\mathrm{c}}(r_{\mathrm{c}})$, when the center of the subunit and the surface of

the nanoparticle are separated by $(2^{1/6}-0.5)\sigma$, and maintains the short range nature of the interactions considered in Ref. [26]. This potential mimics core-subunit interactions that do not favor particular subunit orientations; we consider electrostatic interactions that depend on subunit orientations in a future work. The core-subunit interaction free energy $g_c \equiv \varepsilon_c - Ts_{ad}$ includes an entropy penalty s_{ad} for frozen degrees of freedom in the direction normal to the surface. We determine s_{ad} by calculating the partition function of an adsorbed subunit according to Eq. (7); the result varies weakly with the adsorption energy: $1 < -s_{ad}/k_B < 2.4$ for $3 \leq \varepsilon_c \leq 12$.

Subunit reservoir. We represent a nanoparticle immersed in bulk solution without explicitly simulating thousands of subunits by coupling dynamical simulations to a reservoir of subunits at constant chemical potential. We divide the simulation box into a "main" region centered around the core, where ordinary dynamics are performed, and an outer "bath" region where, in addition to ordinary dynamics, subunits are inserted or deleted in grand canonical Monte Carlo moves [80]. The main region is chosen to have a side length of $L_m = 15\sigma$, which is large enough that subunits cannot simultaneously interact with the nanoparticle and a subunit in the bath area, while the bath has a width of $L_b = 3\sigma$, so the overall box size is $L_m + L_b = 18\sigma$. Insertions and deletions are attempted with a frequency consistent with the diffusion-limited rate for a spherical volume with a diameter of $L_m + L_b$. As assembly proceeds, the concentration of free subunits is depleted and the bath chemical potential should be updated self-consistently. In this work, we consider assembly around a single nanoparticle in infinite dilution (i.e., $C_C = 0$) at system parameters for which little or no spontaneous assembly occurs away from cores, as we will see in the next section. Hence, the chemical potential remains constant.

III. RESULTS

We have simulated assembly dynamics over ranges of subunit concentrations C_S, binding energies ε_b, subunit specificity parameters θ_m, and surface attraction strengths ε_c. All simulations use $\phi_m = \pi$ and $R_C = 1.2$. Other parameter values used in this work are shown in Table I.

TABLE I. Parameter values used for dynamical simulations in this work, where σ is the unit of length, k_BT is the thermal energy, D is the subunit diffusion constant, and $t_0 \equiv \sigma^2/(48D)$ is the unit time.

Parameter	Value	Definition
ε_b/k_BT	6–14	Attractive energy strength, Eq. (3)
b/σ	$2^{-5/6}$	Bond vector length
ϕ_m (rad)	π	Maximum dihedral angle, Eq. (1)
θ_m (rad)	0.25–2.5	Maximum bond angle, Eq. (1)
ε_c/k_BT	4–12	Subunit-core energy, Eq. (7)
R_c/σ	1.2	Core radius, Eq. (7)
L_m/σ	15	Size of main simulation box
L_b/σ	3	Width of bath region
N	30	Number of subunits in a capsid
$C_S = \rho\sigma^3$	2×10^{-3}–0.04	Concentration of subunits in reservoir
r_c/σ	2.5	Attractive energy cutoff distance
t_f/t_0	48 000–600 000	Final observation time

A. The kinetics of core-controlled assembly

In this section we present simple scaling arguments for the effect of core-subunit interactions on the kinetics of assembly and illustrate scaling in simulation assembly trajectories. We first concentrate on the average time to form a capsid, starting from unassembled subunits. As shown by Zlotnick and co-workers [48,53], the assembly of empty capsids can often be broken into nucleation and elongation phases. We show in the Appendix that the average time scales of these phases for an individual capsid can be described by $\tau = \tau_{nuc} + \tau_{elong}$, with $\tau_{nuc}^{-1} \propto f C_S^{n_{nuc}}$ and $\tau_{elong}^{-1} \approx C_S f/(N - n_{nuc})$, where f is the subunit-subunit binding rate constant, C_S is the concentration of free subunits, and n_{nuc} is the number of subunits in the nucleus. Because elongation requires $N - n_{nuc}$ assembly events, it introduces a minimum time scale for the overall assembly process, which is primarily responsible for the lag time in assembly kinetics reported in experiments [9,12,53], theory [21,48], and simulations [26,28,81], and results in a distribution of assembly times for an individual capsid that cannot be fitted with a sum of pure exponential functions [82]. The observed assembly rate constant f can be considered an average quantity, since computational models [26,28] suggest that it varies for different intermediates and decreases due to excluded volume constraints as assembly nears completion. In one model [28], insertion of the final subunit is slow compared to the rest of the elongation and thus introduces a third time scale. Zandi, van der Schoot, and co-workers use continuum theory approaches to analyze nucleation [83] and capsid formation rates at long times [31]. Their finding that the total rate of capsid formation is proportional to C_S^2 at long times is consistent with the time scales given above for a single capsid if elongation dominates.

1. Assembly rates on cores

As we will see from the simulations described below, the presence of cores modifies the nucleation and elongation time scales and introduces a new one, which describes the adsorption of subunits to the core surface. In this discussion we assume that cores are commensurate with the size and geometry of capsids; we discuss the general case elsewhere. If there is no assembly of adsorbed subunits, the equilibrium surface concentration of subunits can be calculated for Langmuir adsorption

$$c_{surf} = C_S \exp(-\beta g_c)/[1 + C_S \exp(-\beta g_c)], \tag{8}$$

where $\beta = 1/k_BT$ is the inverse of the thermal energy, and g_c is the surface-subunit free energy. The adsorption time scale is $\tau_{ad} = n_s/k_{ad}C_S$, with k_{ad} the adsorption rate constant, and the number of adsorbed subunits at saturation, $n_s = N\sigma^3 c_{surf}$. Adsorption will usually be fast compared to assembly rates, which are slow compared to the diffusion-limited rate for protein collisions [53]. Simulation results demonstrate fast

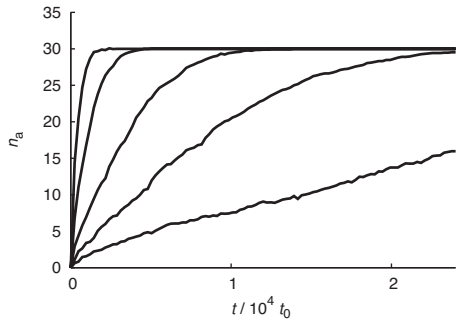

FIG. 2. Time dependence of adsorbed subunits n_a from simulations with varying subunit concentrations. The surface free energy is $\varepsilon_c=7$ ($g_c=-5.1$), the specificity is $\theta_m=1$, and the binding energy is $\varepsilon_b=10$. Curves at increasing height correspond to reduced subunit concentrations of $10^3 C_S=2.04, 4.07, 8.14, 20.4, 40.7$. Each curve is averaged over 60 independent trajectories.

adsorption; Fig. 2 shows the number of adsorbed subunits, n_a, as a function of time for several subunit concentrations. In each case, there is a rapid initial rise in the number of adsorbed subunits, due to nonspecific subunit adsorption (i.e., without binding to other subunits) followed by simultaneous assembly and adsorption until a complete capsid is formed.

For fast adsorption, nucleation takes place at an effective surface concentration of c_{surf} with a time scale

$$\tau_{nuc}^{core} = f_{surf} c_{surf}^{-n_{nuc}}, \tag{9}$$

where we define the surface assembly rate constant $f_{surf} = fD_C/D$, with D and D_C the diffusion constants for free and adsorbed subunits, respectively. We assume that the association rate is proportional to the frequency of subunit collisions because the reaction follows second-order kinetics. The frequency of subunit collisions can be calculated from the Smoluchowski equation for the diffusion-limited rate in three dimensions, with the density of subunits $\rho_{3D}=c_{surf}/\sigma^3$ within a layer above the surface with thickness of the subunit size σ, or from the diffusion-limited rate in two dimensions [84] with a surface density given by $\rho_{2D}=c_{surf}/\sigma^2$. The result of the two calculations differs only by a logarithmic factor that is of order 1 in this case (see Appendix B of Ref. [84]). In simulations for this work $D_C=D$ because subunit friction is isotropic, but we will explore the effects of impeded surface diffusion elsewhere.

Desorption of a nucleated intermediate is unlikely, since it would require breaking multiple subunit-subunit or subunit-core interactions. Assembly therefore leads to a positive flux of adsorbed subunits and elongation occurs at roughly the same concentration c_{surf} with a time scale

$$\tau_{elong}^{core} \approx (N-n_s)/k_{ad}C_S + (N-n_{nuc})/f_{surf}c_{surf}. \tag{10}$$

The first term on the right-hand side of Eq. (10) is the time for the remaining subunits to adsorb to the core surface while the second term accounts for the elongation reaction time.

Equations (9) and (10) predict that cores enhance assembly rates by a factor

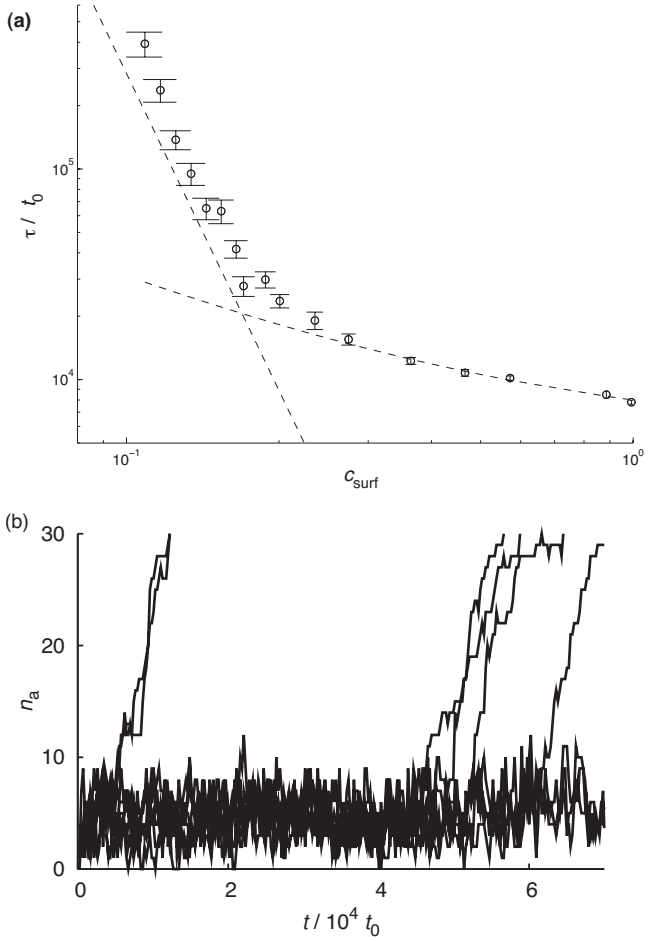

FIG. 3. (a) Average assembly time τ for simulations of core encapsidation for varying surface energies plotted as a function of the surface concentration c_{surf}, described in the text. Simulated surface energies spanned $\varepsilon_c \in [4.1, 12]$, giving surface free energies of $-g_c \in [2.7, 9.6]$. The upper dashed line is a guide to the eye that indicates a nucleation-dominated scaling of c_{surf}^5, while the lower dashed line is a fit to the rightmost four data points with the form $\tau = A + B/c_{surf}$ to illustrate the elongation-dominated scaling. Data points represent an average of 30 or more independent encapsidation trajectories, run at parameter values of $C_S = 8 \times 10^{-3}$, $\varepsilon_b = 10$, and $\theta_m = 1$. (b) Nine individual trajectories are shown for a surface energy in the nucleation regime, $\varepsilon_c = 4.5$ ($c_{surf} = 0.15$).

$$\tau/\tau^{core} = \frac{\tau_{nuc} + \tau_{elong}}{N/k_{ad}C_S + \tau_{nuc}^{core} + \tau_{elong}^{core}}, \tag{11}$$

and that the relative time scales for nucleation and elongation can be manipulated by varying the surface-subunit free energy, to yield regimes in which either nucleation or elongation is rate limiting. Figure 3 shows average assembly times for core encapsidation in simulations at varying surface energies $4.1 \le \varepsilon_c / k_B T \le 12$; the upper and lower dashed lines identify the scaling relations predicted by Eqs. (9) and (10) for nucleation- and elongation-dominated regimes, respectively, and we take $n_{nuc}=5$, although more data would be required to precisely estimate the nucleation size. In addition, the scaling relation is limited in range because the nucleation size can increase at very low ε_c. The nucleus usu-

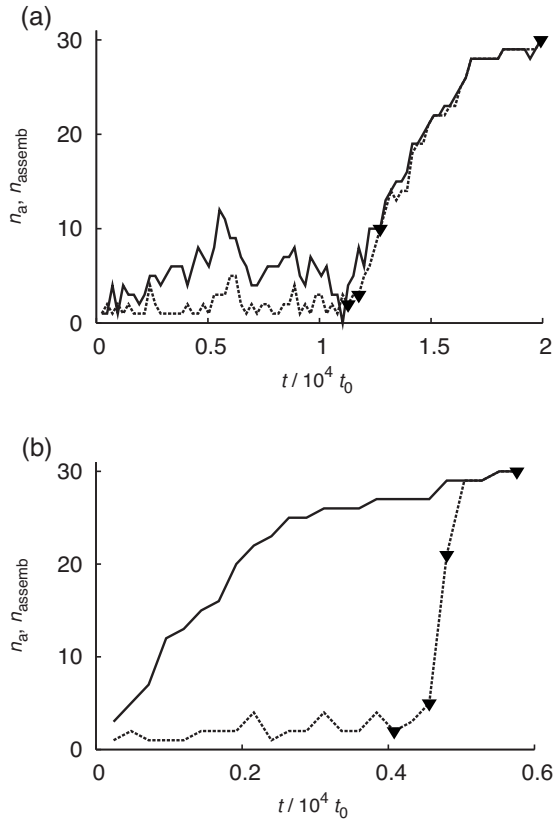

FIG. 4. Time dependences of the total number of adsorbed subunits, n_a (solid lines), and the largest assembled cluster, n_{assemb} (dashed lines), revealing different assembly mechanisms. The subunit concentration is $C_S=8\times10^{-3}$, and the energy parameters are (a) low surface energy and moderate binding energy, $\varepsilon_c=4.5$, $\varepsilon_b=10$; (b) high surface energy and low binding energy, $\varepsilon_c=12$, $\varepsilon_b=7$. The points labeled with (▼) in (a) and (b) correspond to the structures shown in Figs. 5(a) and 5(b), respectively.

ally corresponds to a small polygon in our simulations (see Fig. 5), but the size and geometry of nuclei depend on system parameters. Time series of n_a (the total number of adsorbed subunits) from individual trajectories in the nucleation-dominated regime are shown in Fig. 3(b) to illustrate the stochastic nature of the nucleation event.

2. Cooperative assembly

For large surface free energies, $c_{surf}\approx 1$, meaning that adsorption does not saturate until enough subunits have adsorbed to form a capsid, $n_s\approx N$. Assembly in this regime can occur through a collective reorientation of adsorbed subunits; at low subunit-subunit binding energies (ε_b) this process typically takes place well after adsorption has saturated and thus resembles the reverse micelle assembly mechanism suggested by McPherson [68]. The time dependences of the number of adsorbed subunits, n_a, and the number of assembled subunits, n_{assemb}, are shown for representative trajectories that illustrate the different assembly pathways in Fig. 4, and structures from these trajectories are shown in Fig. 5.

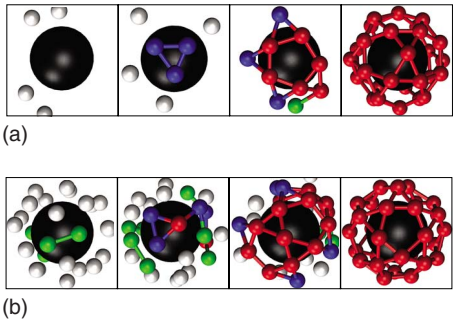

FIG. 5. (Color online) Snapshots from the simulation trajectories shown in Fig. 4(a), illustrating two assembly mechanisms: (a) sequential assembly at low surface energy, $\varepsilon_c=4.5$, and (b) cooperative assembly at high surface energy, $\varepsilon_c=12$. Snapshots from right to left correspond to increasing time and correspond to the triangles shown in (a) Fig. 4(a) and (b) Fig. 4(b). The size of subunits is reduced to aid visibility, and subunit color indicates the number of complementary interactions: white, 0; green (light gray), 1; blue (dark gray), 2; red (darkest gray) 3 or 4. All images of simulation structures in this work were generated with VMD [85].

B. Packaging efficiencies

In addition to enhancing and controlling rates of assembly, cores can increase assembly yields. As a measure of efficiency of assembly, we observe packaging efficiencies, which are defined as the fraction of independent trajectories for which a nanoparticle is encapsidated by a perfect capsid. A "perfect capsid" is comprised of 30 subunits, each of which has the maximum number of bonds (4). The variation of packaging efficiencies with binding energy is shown in Fig. 6 for an observation time of $t_f=48\,000$, beyond which packaging efficiencies increase only slowly.

1. Core control of assembly through heterogeneous nucleation

At the subunit concentration considered in Fig. 6, $C_S=8\times10^{-3}$, spontaneous assembly into properly formed empty

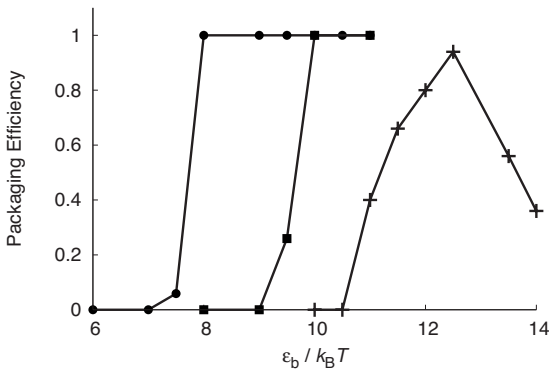

FIG. 6. Efficiency of encapsidation of a model nanoparticle is compared to the fraction of subunits in capsids due to spontaneous assembly of empty capsids, shown with symbol (+). Packaging efficiencies, or the fraction of independent trajectories in which a nanoparticle was encapsidated by a perfect capsid, are shown for neutral subunits at $\varepsilon_c=7$ (■) and $\varepsilon_c=12$ (●), with a subunit concentration of $C_S=8\times10^{-3}$ and a final observation time of $t_f=48\,000$. Spontaneous assembly results are shown at $C_S=0.11$ and $t_f=600\,000$. The specificity parameter $\theta_m=0.5$ for all points.

capsids is not observed for any of the binding energies considered, while cores are efficiently encapsidated over a relatively wide range of ε_b. This observation is consistent with experiments, which find that assembly occurs in the presence of nanoparticles below the critical subunit concentration at which spontaneous assembly occurs [69]. Model nanoparticles enhance assembly because favorable core-subunit interactions lead to a high local concentration c_{surf} of "adsorbed" subunits near core surfaces [see Eq. (8)]. Assembly and encapsidation occur when the effective surface concentration exceeds the CSC ($c_{surf} > \mathrm{CSC}$). Core encapsidation simulations were not carried out at binding energies of $\varepsilon_b > 11$ to ensure that there was no assembly in the bath. At higher binding energies, spontaneous assembly is rapid and depletes the concentration of free subunits, and thus suppresses nanoparticle encapsidation and decreases packaging efficiencies. The competition between core-controlled and spontaneous assembly will be explored in a future work.

Assembly on cores is robust in the sense that packaging efficiencies remain near 100% over wide ranges of the subunit binding energy ε_b and the surface attraction energy ε_c. As a comparison, we consider independent simulations of empty capsid assembly (without model nanoparticles) at a subunit concentration of $C_S=0.11$ for which spontaneous assembly is relatively productive [86]. As a measure of assembly effectiveness in empty capsid simulations, we define the "packaging efficiency" as the fraction of subunits in complete capsids. At an observation time of $t_f/t_0=6\times10^5$, approximately 12 times longer than the observation time for core encapsidation, efficient assembly occurs over the relatively narrow range of $11.0 \lesssim \epsilon_b \lesssim 13.5$. Empty capsid assembly is thwarted by two forms of kinetic trap at higher values of subunit-subunit binding energies. If new assembly intermediates form too rapidly, the pool of free subunits becomes depleted before most capsids finish assembling [12,21,26,47,48,52,53], and malformed structures result when additional subunits bind more rapidly than strained bonds can anneal within a partial capsid [26,28,55,56]. Cores suppress the first of these traps by enabling rapid assembly well below the CSC, so that the number of nucleation sites is controlled by the concentration of cores even during rapid assembly.

2. Core control of assembly through templating

The formation of misbonded configurations impedes assembly when subunit-subunit binding energies are large compared to k_BT, because progression from these configurations to a properly formed capsid requires unbinding events and thus is characterized by large activation energies. An interior core could suppress this form of kinetic trap by acting as a template that directs assembly at all stages toward a morphology consistent with the low free energy capsid. We explore this capability by varying the subunit specificity parameter θ_m, which controls the intrinsic likelihood of subunits to form strained bonds (see Sec. II A).

As shown in Fig. 7, efficient spontaneous assembly of empty capsids occurs over the relatively narrow range of $0.5 \lesssim \theta_m \lesssim 1.0$. At low values of θ_m, subunit binding rates are prohibitively slow because most collisions do not lead to bond formation, while at larger values of θ_m strained bonds tend to be trapped within growing capsids. The presence of assemblages with strained bonds and the lack of free subunits are illustrated by a snapshot from the end of a simulation with $\theta_m=2.0$ in Fig. 8(a); a snapshot at the end of a core simulation is shown in Fig. 8(b) for comparison.

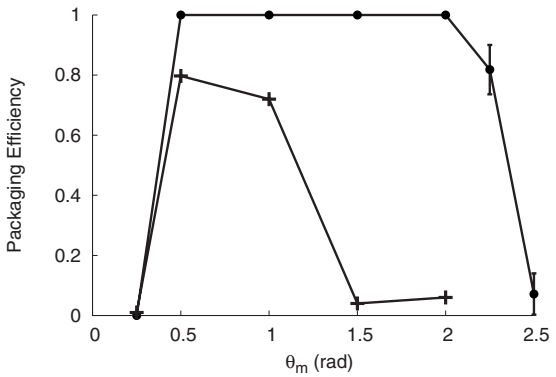

FIG. 7. (a) Variation of assembly with specificity parameter θ_m. Packaging efficiencies (●) are shown for $\varepsilon_b=10$, $C_S=8\times10^{-3}$, and $t_f=48\,000$, while the fractions of subunits in empty capsids (+) are shown for $\varepsilon_b=12$, $C_S=0.11$, and. $t_f=240\,000$.

Core-controlled assembly, on the other hand, results in packaging efficiencies near 100% for specificity parameters as large as $\theta_m=2.25$. Because the core is commensurate with the size of a perfect capsid, subunits are driven to bind with the correct local curvature at all stages of the assembly process. Note that the core simulations in Fig. 7 benefit from heterogeneous nucleation as well as templating; subunit binding rates and free energies increase with θ_m, and thus so do spontaneous nucleation rates. We determine that templating becomes increasingly important as θ_m rises because empty capsid simulations with $\theta_m \geq 1.5$ yield a significant fraction of malformed structures. Simulations in which there is heterogeneous nucleation but no templating show a similar sensitivity to θ_m as empty-capsid simulations.

IV. DISCUSSION

In this work we present scaling arguments and simulations that describe the assembly of capsid protein subunits around rigid cores. The kinetics and efficiency of assembly are predicted as functions of subunit-subunit binding energies, subunit concentrations and subunit-core interaction strengths. We find that assembly pathways depend sensitively on the strength of subunit-core interactions. For weak attractions, capsid formation requires assembly of adsorbed subunits into a stable intermediate, followed by sequential adsorption and assembly of individual subunits. Strong interactions induce rapid adsorption resulting in nearly complete, but disordered, monolayers of subunits, followed by cooperative subunit reordering to form capsids. Variations in assembly mechanisms are revealed by the time dependence of adsorbed subunits, as shown in Fig. 2, and by the scaling of assembly times with subunit concentration, as shown in Fig. 3.

Model predictions for the variation of assembly timescales and packaging efficiencies with subunit concentration

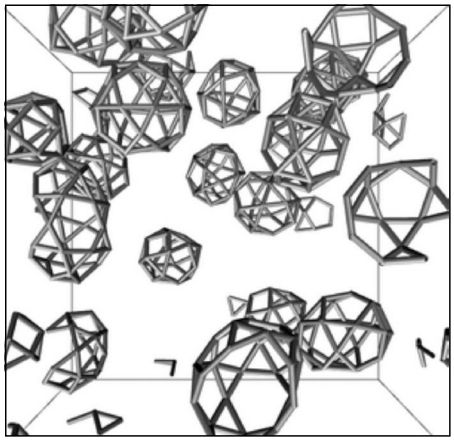

(a)

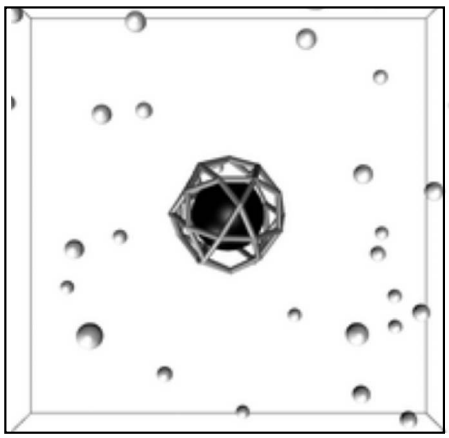

(b)

FIG. 8. (a) Snapshot of part of the simulation box at the end of an empty capsid simulation with $\theta_m=2$ for the parameters in Fig. 7. Some capsids are closed but strained, as indicated by the presence of hexagons or squares. (b) Snapshot at the end of the core encapsidation trajectory shown in Fig. 5(a).

C_S and core-subunit interaction strengths g_c can be verified in viruslike particle assembly experiments. The parameter g_c can be related to the experimentally controlled functionalized surface charge density. Protein adsorption and assembly kinetics can be monitored with time resolved light scattering [69], and packaging efficiencies can be determined from transmission electron microscopy (TEM) micrographs [33]. Successful validation of model predictions would provide strong evidence for the control of assembly mechanisms by a templating component, which prior works suggest is important for understanding viral assembly *in vivo* [59,68].

A. Implications for designing and understanding assembly reactions

Experiments [12,55] and models [21,26,28,48,52,81] show that subunits can spontaneously assemble into low free energy ordered states with high yield and selectivity, but that effective assembly is limited to optimal ranges of the forces that drive assembly. For nonoptimal interactions, assembly is either not thermodynamically favored, or thwarted by long-lived disordered states. These limitations of spontaneous assembly have shaped the evolution of assembling components in biological systems, and similarly constrain the development of assembled nanostructured materials. Our results suggest that cooperative interactions between disparate assembling components offer the potential to circumvent some limitations of spontaneous assembly, particularly through heterogeneous nucleation and templating.

The novel mechanisms and capabilities of multicomponent assembly introduce new considerations for the design of assembly processes. For example, Zlotnick and co-workers [53] show that a slow nucleation step in the spontaneous assembly of empty capsids can suppress kinetic traps. This condition is met for some parameter values of our simulation model—initial assembly steps can be slow in comparison to later ones because subunits in small intermediates have few bonds. As subunit-subunit binding energies are decreased these initial steps become even slower; however, the capsid products are less thermodynamically stable and subsequent elongation rates can also decrease, resulting in increased assembly times. Introducing cores to the simulations provides an independent means to control the formation of assembly nuclei while still enabling fast elongation kinetics, and thereby promotes rapid assembly with high yield and selectivity.

Controling assembly kinetics by changing the properties of a template component will be useful for designing synthetic or biomimetic assembly reactions for which it is impractical to change the molecular structure of subunits or environmental conditions. For example, protein-protein interactions, and hence the critical subunit concentration, can be controlled in viruslike particle experiments by varying the salt concentration or *p*H [12,29,47]. Capsid proteins denature, however, if these parameters are changed too far from physiological conditions. Our results suggest that varying the functionalized surface charge density on nanoparticles enables independent control over the CSC and packaging efficiencies. Similarly, viruses have limited capability to control the cellular environments in which they replicate, and amino acids at capsid protein-protein interfaces are highly conserved, perhaps in part because the need for capsid dissociation upon infecting a new cell constrains these interactions. Interactions between capsid proteins and the viral genome or host cellular compenents may provide important alternative avenues to promote and control assembly, and hence viral replication.

V. OUTLOOK

A. Core-assembly geometry incompatibility

Our models describe encapsidation of cores with shapes and sizes commensurate with the low free energy capsid product. The simulation results demonstrate that the influence of core curvature on local subunit-subunit bonding configurations can dramatically influence global capsid morphologies (see Fig. 7). Core curvature that is inconsistent

with the lowest free energy subunit-subunit bonding configurations will introduce frustration and thus may limit the robustness of assembly. Experimental observations that solid cores [33] and nucleic acid cores [87] with different sizes promote assembly of different capsid morphologies demonstrate that frustration is an important consideration in biological and nanostructured assembly processes. Comparison of our current model with experimental results will identify frustration and future work will explicitly address geometrical frustration. Additionally, physioadsorption of subunits on core surfaces could impede lateral diffusion and thereby promote kinetic traps. However, simulations in which adsorbed subunits had friction constants increased by a factor of 100 in directions tangential to the core surface demonstrated only a small increase in propensity for kinetic traps, although net assembly rates were slower.

B. Fluctuating cores

Cores comprised of nucleic acids or other macromolecules with dynamic configurations can change size and shape during encapsidation. Although the time scale arguments presented in Eqs. (9) and (10) can be generalized to include an additional time scale that represents core dynamics, the possibility of additional forms of kinetic traps due to fluctuating core configurations should be explored.

VI. CONCLUSIONS

In summary, we have presented simulations and scaling arguments that describe the assembly of solubilized subunits around rigid cores. These models mimic the dynamical assembly of viral capsid proteins around functionalized inorganic nanoparticles, but are general enough for broad applicability in describing the assembly of biological or nanostructured materials around templates. We find that template properties can dramatically influence assembly time scales and mechanisms, as evidenced by the prediction of an assembly mechanism not seen during the assembly of empty capsids. These conclusions may be significant for understanding the role of nucleic acids in the viral assembly and for designing nanomaterials or drug delivery vehicles to interact with cargo molecules.

ACKNOWLEDGMENTS

I gratefully acknowledge Rob Jack and Bogdan Dragnea for insightful discussions during this work, Aaron Dinner, Bulbul Chakraborty, and Jane' Kondev for critical readings of the manuscript, and Oren Elrad for assistance in preparing the manuscript. Funding was provided by an HHMI-NIBIB Interfaces Initiative grant to Brandeis University and Brandeis University startup funds.

APPENDIX

In this appendix we estimate the average time scale for an individual capsid to assemble. We follow Zlotnick and coworkers [21,48,53] and describe assembly as a sequence of reversible additions of individual subunits to a growing capsid, with the assembly broken into a nucleation phase and an elongation phase. To simplify the analysis, we consider the beginning stages of assembly and assume that the concentration of free subunits, C_S, remains constant during the formation of an individual capsid, and consider the following reaction:

$$1 \underset{b_{nuc}}{\overset{fC_S}{\rightleftharpoons}} 2 \underset{b_{nuc}}{\overset{fC_S}{\rightleftharpoons}} \cdots \underset{b_{nuc}}{\overset{fC_S}{\rightleftharpoons}} n_{nuc} \underset{b_{elong}}{\overset{fC_S}{\rightleftharpoons}} \cdots \underset{b_{elong}}{\overset{fC_S}{\rightleftharpoons}} N, \tag{A1}$$

where b_i is the dissociation rate constant (with $i=\{\mathrm{nuc},\mathrm{elong}\}$), which is related to the forward rate constant by detailed balance, $b_i=f\exp(G_i/k_BT)$, with G_i the subunit association free energy. The two phases are distinguished by the fact that association in the nucleation phase is not free energetically favorable, $C_S\exp(-G_{nuc}/k_BT)<1$, while association in the elongation phase is favorable, $C_S\exp(-G_{elong}/k_BT)>1$. Nucleation in our simulations typically corresponds to the formation of a closed polygon of a certain size, so that every subunit in the intermediate has at least two bonds.

For simplicity, we assume that the forward rate constant f is the same for all reactions and all subunit association free energies within a phase (nucleation or elongation) are equal. The average time for a capsid to complete the nucleation phase can be calculated from the mean first passage time for a biased random walk with a reflecting boundary conditions at 1 and absorbing boundary conditions at n_{nuc}, with forward and reverse hopping rates given by fC_S and b_{nuc}, respectively [88],

$$t_{nuc}=\frac{n_{nuc}}{fC_S-b_{nuc}}-\left(\frac{b_{nuc}}{fC_S-b_{nuc}}\right)^2\left(\frac{b_{nuc}}{fC_S}\right)^{n_{nuc}}. \tag{A2}$$

In the limit $fC_S \ll b_{nuc}$ Eq. (A2) can be approximated to give $t_{nuc}^{-1}\approx f\exp[-(n_{nuc}-1)\,G_{nuc}/k_BT)]C_S^{n_{nuc}}$, which was derived in the appendix of Ref. [48].

The time scale for the elongation phase follows by the same analysis and can be obtained from Eq. (A2) by replacing b_{nuc} with b_{elong} and n_{nuc} with $N-n_{nuc}$. In the limit of $fC_S \gg b_{elong}$ Eq. (A2) can be approximated to give $t_{elong}\approx(N-n_{nuc})/fC_S$, while similar forward and reverse reaction rates, $fC_S\approx b_{elong}$, give $t_{elong}\approx(N-n_{nuc})^2/2fC_S$.

Equation (A1) can be solved exactly, and the first capsids appear after a lag time equal to the elongation time t_{elong}. (The same lag time occurs if the complete set of rate equations, which include depletion of monomers, are integrated.) In Zlotnick and co-workers' formulation, the nucleation and elongation phases are distinguished by having different forward rate constants rather than different association free energies. The analysis in that case is similar.

If nucleation is fast compared to elongation, $Nt_{elong}\gtrsim t_{nuc}$, the assumption that the free subunit concentration is constant will be invalid, subunits will be depleted before most capsids finished assembling, and the reaction will be kinetically trapped.

[1] S. C. Glotzer, Science **306**, 419 (2004).
[2] G. M. Whitesides and B. Grzybowski, Science **295**, 2418 (2002).
[3] T. Douglas and M. Young, Science **312**, 873 (2006).
[4] C. Valery *et al.*, Proc. Natl. Acad. Sci. U.S.A. **100**, 10258 (2003).
[5] H. Yan, S. H. Park, G. Finkelstein, J. H. Reif, and T. H. LaBean, Science **301**, 1882 (2003).
[6] E. Strable, J. E. Johnson, and M. G. Finn, Nano Lett. **4**, 1385 (2004).
[7] A. S. Blum *et al.*, Nano Lett. **4**, 867 (2004).
[8] J. M. Johnson, J. H. Tang, Y. Nyame, D. Willits, M. J. Young, and A. Zlotnick, Nano Lett. **5**, 765 (2005).
[9] G. L. Casini, D. Graham, D. Heine, R. L. Garcea, and D. T. Wu, Virology **325**, 320 (2004).
[10] S. Singh and A. Zlotnick, J. Biol. Chem. **278**, 18249 (2003).
[11] D. Willits, X. Zhao, N. Olson, T. S. Baker, A. Zlotnick, J. E. Johnson, T. Douglas, and M. J. Young, Virology **306**, 280 (2003).
[12] A. Zlotnick, R. Aldrich, J. M. Johnson, P. Ceres, and M. J. Young, Virology **277**, 450 (2000).
[13] A. Klug, Philos. Trans. R. Soc. London, Ser. B **354**, 531 (1999).
[14] A. Zlotnick, N. Cheng, J. F. Conway, F. P. Booy, A. C. Steven, S. J. Stahl, and P. T. Wingfield, Biochemistry **35**, 7412 (1996).
[15] J. M. Fox, J. E. Johnson, and M. J. Young, Seminars Virol. **5**, 51 (1994).
[16] P. J. G. Butler and A. Klug, Sci. Am. **239**, 62 (1978).
[17] H. Fraenkelconrat and R. C. Williams, Proc. Natl. Acad. Sci. U.S.A. **41**, 690 (1955).
[18] F. H. C. Crick and J. D. Watson, Nature (London) **177**, 473 (1956).
[19] D. L. D. Caspar and A. Klug, Cold Spring Harbor Symp. Quant. Biol. **27**, 1 (1962).
[20] B. Berger, P. W. Shor, L. Tuckerkellogg, and J. King, Proc. Natl. Acad. Sci. U.S.A. **91**, 7732 (1994).
[21] A. Zlotnick, J. Mol. Biol. **241**, 59 (1994).
[22] R. F. Bruinsma, W. M. Gelbart, D. Reguera, J. Rudnick, and R. Zandi, Phys. Rev. Lett. **90**, 248101 (2003).
[23] R. Zandi, D. Reguera, R. F. Bruinsma, W. M. Gelbart, and J. Rudnick, Proc. Natl. Acad. Sci. U.S.A. **101**, 15556 (2004).
[24] T. Keef, A. Taormina, and R. Twarock, Phys. Biol. **2**, 175 (2005).
[25] R. Twarock, Bull. Math. Biol. **67**, 973 (2005).
[26] M. F. Hagan and D. Chandler, Biophys. J. **91**, 42 (2006).
[27] T. Chen and S. C. Glotzer, Phys. Rev. E **75**, 051504 (2007).
[28] H. D. Nguyen, V. S. Reddy, and C. L. Brooks, Nano Lett. **7**, 338 (2007).
[29] W. K. Kegel and P. van der Schoot, Biophys. J. **86**, 3905 (2004).
[30] S. D. Hicks and C. L. Henley, Phys. Rev. E **74**, 031912 (2006).
[31] P. van der Schoot and R. Zandi, Phys. Biol. **4**, 296 (2007).
[32] N. Dimmock, A. Easton, and K. Leppard, *Introduction to Modern Virology* (Blackwell Publishing, Malden, MA, 2001).
[33] J. Sun *et al.*, Proc. Natl. Acad. Sci. U.S.A. **104**, 1354 (2007).
[34] S. K. Dixit, N. L. Goicochea, M. C. Daniel, A. Murali, L. Bronstein, M. De, B. Stein, V. M. Rotello, C. C. Kao, and B. Dragnea, Nano Lett. **6**, 1993 (2006).
[35] C. Chen, E. S. Kwak, B. Stein, C. C. Kao, and B. Dragnea, J. Nanosci. Nanotechnol. **5**, 2029 (2005).
[36] B. Dragnea, C. Chen, E. S. Kwak, B. Stein, and C. C. Kao, J. Am. Chem. Soc. **125**, 6374 (2003).
[37] C. M. Soto, A. S. Blum, G. J. Vora, N. Lebedev, C. E. Meador, A. P. Won, A. Chatterji, J. E. Johnson, and B. R. Ratna, J. Am. Chem. Soc. **128**, 5184 (2006).
[38] K. E. Sapsford, C. M. Soto, A. S. Blum, A. Chatterji, T. W. Lin, J. E. Johnson, F. S. Ligler, and B. R. Ratna, Biosens. Bioelectron. **21**, 1668 (2006).
[39] Z. Boldogkoi, A. Sik, A. Denes, A. Reichart, J. Toldi, I. Gerendai, K. J. Kovacs, and M. Palkovits, Prog. Neurobiol. **72**, 417 (2004).
[40] B. Gupta, T. S. Levchenko, and V. P. Torchilin, Adv. Drug Delivery Rev. **57**, 637 (2005).
[41] R. L. Garcea and L. Gissmann, Curr. Opin. Biotechnol. **15**, 513 (2004).
[42] G. P. H. Dietz and M. Bahr, Mol. Cell. Neurosci. **27**, 85 (2004).
[43] A. Chatterji, W. F. Ochoa, T. Ueno, T. W. Lin, and J. E. Johnson, Nano Lett. **5**, 597 (2005).
[44] J. C. Falkner, M. E. Turner, J. K. Bosworth, T. J. Trentler, J. E. Johnson, T. W. Lin, and V. L. Colvin, J. Am. Chem. Soc. **127**, 5274 (2005).
[45] C. E. Flynn, S. W. Lee, B. R. Peelle, and A. M. Belcher, Acta Mater. **51**, 5867 (2003).
[46] T. Douglas and M. Young, Nature (London) **393**, 152 (1998).
[47] P. Ceres and A. Zlotnick, Biochemistry **41**, 11525 (2002).
[48] D. Endres and A. Zlotnick, Biophys. J. **83**, 1217 (2002).
[49] D. C. Rapaport, J. E. Johnson, and J. Skolnick, Comput. Phys. Commun. **121-122**, 231 (1999).
[50] D. C. Rapaport, Phys. Rev. E **70**, 051905 (2004).
[51] D. Rapaport, e-print arXiv:0803.0115v1.
[52] T. Q. Zhang and R. Schwartz, Biophys. J. **90**, 57 (2006).
[53] A. Zlotnick, J. M. Johnson, P. W. Wingfield, S. J. Stahl, and D. Endres, Biochemistry **38**, 14644 (1999).
[54] B. Sweeny, T. Zhang, and R. Schwartz, Biophys. J. **94**, 772 (2008).
[55] P. K. Sorger, P. G. Stockley, and S. C. Harrison, J. Mol. Biol. **191**, 639 (1986).
[56] R. Schwartz, P. W. Shor, P. E. Prevelige, and B. Berger, Biophys. J. **75**, 2626 (1998).
[57] R. L. Jack, M. F. Hagan, and D. Chandler, Phys. Rev. E **76**, 021119 (2007).
[58] G. M. Whitesides and M. Boncheva, Proc. Natl. Acad. Sci. U.S.A. **99**, 4769 (2002).
[59] J. M. Johnson, D. A. Willits, M. J. Young, and A. Zlotnick, J. Mol. Biol. **335**, 455 (2004).
[60] D. G. Angelescu, R. Bruinsma, and P. Linse, Phys. Rev. E **73**, 041921 (2006).
[61] P. van der Schoot and R. Bruinsma, Phys. Rev. E **71**, 061928 (2005).
[62] D. Q. Zhang, R. Konecny, N. A. Baker, and J. A. McCammon, Biopolymers **75**, 325 (2004).
[63] T. Hu, R. Zhang, and B. I. Shklovskii, e-print arXiv:cond-mat/0610009v4.
[64] V. A. Belyi and M. Muthukumar, Proc. Natl. Acad. Sci. U.S.A. **103**, 17174 (2006).
[65] T. Chen, Z. L. Zhang, and S. C. Glotzer, Proc. Natl. Acad. Sci. U.S.A. **104**, 717 (2007).
[66] J. Rudnick and R. Bruinsma, Phys. Rev. Lett. **94**, 038101

(2005).
[67] T. Hu and B. I. Shklovskii, Phys. Rev. E **75**, 051901 (2007).
[68] A. McPherson, Bioessays **27**, 447 (2005).
[69] B. Dragnea, (private communication).
[70] A. van Blaaderen, Nature (London) **439**, 545 (2006).
[71] Z. F. Li, D. Y. Lee, M. F. Rubner, and R. E. Cohen, Macromolecules **38**, 7876 (2005).
[72] Y. S. Cho, G. R. Yi, J. M. Lim, S. H. Kim, V. N. Manoharan, D. J. Pine, and S. M. Yang, J. Am. Chem. Soc. **127**, 15968 (2005).
[73] P. Pfeiffer and L. Hirth, Virology **61**, 160 (1974).
[74] M. Cuillel, M. Zulauf, and B. Jacrot, J. Mol. Biol. **164**, 589 (1983).
[75] C. Berthetcolominas, M. Cuillel, M. H. J. Koch, P. Vachette, and B. Jacrot, Eur. Biophys. J. **15**, 159 (1987).
[76] K. N. Parent, M. M. Suhanovsky, and C. M. Teschke, J. Mol. Biol. **365**, 513 (2007).
[77] P. E. Prevelige, D. Thomas, and J. King, Biophys. J. **64**, 824 (1993).
[78] R. W. Lucas, S. B. Larson, and A. McPherson, J. Mol. Biol. **317**, 95 (2002).
[79] P. Natarajan, G. C. Lander, C. M. Shepherd, V. S. Reddy, C. L. Brooks, and J. E. Johnson, Nat. Rev. Microbiol. **3**, 809 (2005).
[80] D. Frenkel and B. Smit, *Understanding Molecular Simulation: from Algorithms to Applications*, 2nd ed. (Academic, San Diego, CA, 2002).
[81] A. W. Wilber, J. P. K. Doye, A. A. Louis, E. G. Noya, M. A. Miller, and P. Wong, J. Chem. Phys. **127**, 085106 (2007).
[82] E. Kamber, J. Kondev, and M. F. Hagan (unpublished).
[83] R. Zandi, P. van der Schoot, D. Reguera, W. Kegel, and H. Reiss, Biophys. J. **90**, 1939 (2006).
[84] H. C. Berg and E. M. Purcell, Biophys. J. **20**, 193 (1977).
[85] W. Humphrey, A. Dalke, and K. Schulten, J. Mol. Graphics **14**, 33 (1996).
[86] The empty capsid simulations did not use a subunit bath; 500 subunits were simulated in a box with side length 16.67 σ.
[87] M. A. Krol, N. H. Olson, J. Tate, J. E. Johnson, T. S. Baker, and P. Ahlquist, Proc. Natl. Acad. Sci. U.S.A. **96**, 13650 (1999).
[88] A. Bar-Haim and J. Klafter, J. Comput. Phys. **109**, 5187 (1998).